

# Li-ViP3D++: Query-Gated Deformable Camera–LiDAR Fusion for End-to-End Perception and Trajectory Prediction

Matej Halinkovic\*, Nina Masarykova\*, Alexey Vinel†‡, Marek Galinski\*

† Karlsruhe Institute of Technology, Kaiserstraße 89, 76133 Karlsruhe, Germany

\* Slovak University of Technology, Ilkovičova 2, 842 16 Bratislava, Slovakia

‡ Halmstad University, Kristian IV:s väg 3, 301 18 Halmstad, Sweden

Email: {matej.halinkovic, nina.masarykova, marek.galinski}@stuba.sk, alexey.vinel@kit.edu

**Abstract**—End-to-end perception and trajectory prediction from raw sensor data is one of the key capabilities for autonomous driving. Modular pipelines restrict information flow and can amplify upstream errors. Recent query-based, fully differentiable perception-and-prediction (PnP) models mitigate these issues, yet the complementarity of cameras and LiDAR in the query-space has not been sufficiently explored. Models often rely on fusion schemes that introduce heuristic alignment and discrete selection steps which prevent full utilization of available information and can introduce unwanted bias. We propose Li-ViP3D++, a query-based multimodal PnP framework that introduces Query-Gated Deformable Fusion (QGDF) to integrate multi-view RGB and LiDAR in query space. QGDF (i) aggregates image evidence via masked attention across cameras and feature levels, (ii) extracts LiDAR context through fully differentiable BEV sampling with learned per-query offsets, and (iii) applies query-conditioned gating to adaptively weight visual and geometric cues per agent. The resulting architecture jointly optimizes detection, tracking, and multi-hypothesis trajectory forecasting in a single end-to-end model. On nuScenes, Li-ViP3D++ improves end-to-end behavior and detection quality, achieving higher EPA (0.335) and mAP (0.502) while substantially reducing false positives (FP ratio 0.147), and it is faster than the prior Li-ViP3D variant (139.82 ms vs. 145.91 ms). These results indicate that query-space, fully differentiable camera–LiDAR fusion can increase robustness of end-to-end PnP without sacrificing deployability.

**Index Terms**—Perception, perception and prediction, machine learning, computer vision, deep learning, multimodality, trajectory prediction.

## I. INTRODUCTION

Forecasting the positions and future behavior of agents in a traffic scene is one of the key capabilities needed for autonomous driving, for road-infrastructure management, and

This work has been submitted to the IEEE for possible publication. Copyright may be transferred without notice, after which this version may no longer be accessible.

This work was funded by the Excellence Strategy of the German Federal and State Governments and the Helmholtz Program “Engineering Digital Futures”. Additionally, it was funded the EU NextGenerationEU through the Recovery and Resilience Plan for Slovakia under the project No. 09I05-03-V02-00014 and by APVV-23-0519 project “Legal and Technical Challenges of Smart Mobility to Increase Road Traffic Safety”. Finally, the support of the ELLIIT strategic research network and the Helmholtz Association Initiative and Networking Fund on the HAICORE@KIT partition is gratefully acknowledged.

ensuring the safety of vulnerable road users. For downstream planning and control, anticipating how surrounding participants will evolve is as important as estimating their current state. As trajectory prediction methods improve in autonomous driving environments, they contribute directly to safer interactions among road users and to smoother traffic flow.

Among Perception and Prediction (PnP) approaches in autonomous driving, the most advanced direction is to predict trajectories directly from raw sensor inputs. Accordingly, end-to-end models that unify object detection, tracking, and prediction have become an important component of embodied perception [1]. However, leading solutions still omit several practical considerations. In particular, there remains a lack of methods that can fully exploit both RGB and LiDAR streams in a single, fully differentiable framework. Although unimodal methods have historically dominated computer vision for dynamic scenes, they exhibit fundamental shortcomings [2], [3]. LiDAR-centric approaches often emphasize computational efficiency, whereas camera-based systems can be deployed using comparatively inexpensive hardware. Despite these advantages, unimodal pipelines inherit the failure modes and constraints of the single sensor they depend on.

These limitations reduce the reliability of PnP systems in challenging conditions that involve diverse object types and changing environments. Recent research has shown that object queries proposed by DETR3D [4], [5], a learned sparse set of embedding vectors (object priors) which can be decoded into a 3D reference point, are an effective interface for using RGB data for 3D detections. Query-based approaches have expanded to showcase the suitability of the interface for object tracking and trajectory prediction [6]. However, while they underline the value of RGB for 3D detection and forecasting, they do not resolve the broader uncertainty issues faced by PnP systems that rely exclusively on vision. This is especially relevant when the goal is to protect vulnerable road users. Recent research on traffic monitoring with social robots [7], [8] indicates that RGB sensing can support basic detection and intention inference, yet it does not provide sufficiently accurate estimates of agent position and timing.

This manuscript extends our earlier proceedings publica-

tion [9]. In that work, we introduced Li-ViP3D, a novel end-to-end and fully differentiable approach to trajectory prediction from combined RGB and LiDAR data. Li-ViP3D expanded the agent-query paradigm into a multimodal framework capable of predicting trajectories over a 6-second horizon for a broad set of agents, including cars, bicycles, and pedestrians. We also redesigned the 3D agent-query interface to incorporate LiDAR information and showed that this interface enables effective fusion of RGB and LiDAR cues.

In the present extension, our primary contributions focus on a new query-gated deformable fusion (QGDF) strategy that further increases the practicality of agent queries for end-to-end perception and prediction. We modify our Li-ViP3D architecture to use the QGDF mechanism. The resulting Li-ViP3D++ network improves computational efficiency and detection quality, while also enhancing the explainability of the base Li-ViP3D.

## II. RELATED WORK

### A. Traditional Perception and Prediction Pipelines

Research on the detection-tracking-forecasting pipeline is extensive and spans many facets of these challenging problems [10]. Although numerous methods address parts of the pipeline, the shift toward fully end-to-end formulations is still in its early stages. As a result, there is not yet broad agreement on how to design end-to-end systems that simultaneously account for the full range of requirements.

Conventional PnP systems typically decompose the task into separate components [11]–[14]: object detection, object tracking, and trajectory prediction. Advocates of modular designs emphasize their adaptability, ease of upgrading individual modules, and clearer attribution of errors, arguing that these benefits can outweigh those of end-to-end models. Many such points are well supported: for example, vehicle recognition can be handled efficiently with lightweight region filtering [15], and geometric cues from camera frames can improve scene understanding [16]. Nevertheless, existing modular pipelines have not yet demonstrated a practical way to counteract the propagation and accumulation of errors across stages when modules are integrated, while still meeting real-time computational constraints. Moreover, modular interfaces typically enforce compact information exchange, often passing only selected descriptors such as position, velocity, acceleration, distance, and related features.

### B. End-to-End solutions

End-to-end formulations, by contrast, can carry informative cues about agent intent from perception to prediction, including signals such as turn indicators and brake lights, as well as body pose and other rich context. They are also appealing from an engineering standpoint due to single-loop training and simpler deployment. However, until recently, methods such as FaF [17], IntentNet [18], and PnPNet [19] did not fully realize the promise of end-to-end PnP, because they depended on intermediate feature-map representations and non-differentiable operations (e.g., non-maximum suppression).

This design choice restricts error propagation between PnP components and often leads to only partial coupling through a composite loss.

Prior work [17], [18], [20] has nevertheless shown that agent intention can be inferred directly from raw sensor inputs. These approaches, however, performed direct prediction without incorporating explicit tracking, which weakened performance on occluded agents and limited the usable sensor history before model saturation.

Contemporary multimodal systems commonly build upon ideas introduced by PnPNet [19]. PnPNet established the feasibility of end-to-end trajectory prediction from raw sensor data for longer-horizon forecasting ( $>1$ s), and it further emphasized the value of separating concerns while including explicit temporal tracking.

The introduction of Visual Trajectory Prediction via 3D agent queries (ViP3D) [6] represented a notable step forward by demonstrating that end-to-end, fully differentiable prediction can be achieved in practice. Its query-based formulation provides a feature- and attention-driven mechanism that propagates perception information throughout the model. Additionally, by avoiding non-differentiable intermediate stages, it became the first fully differentiable vision-based trajectory prediction approach to use rich feature representations as the primary interface.

### C. Attention-based RGB and LiDAR fusion

BEVFusion [21] presents an efficient strategy for lifting 2D camera observations into a 3D bird’s-eye-view representation, enabling trajectory prediction to operate within a shared 3D space across modalities for most of the network. A key outcome is a reported  $40\times$  speedup over the prior standard BEV conversion technique, Lift-Splat-Shoot [22] (LSS). The high cost of BEV conversion previously created a major bottleneck and hindered the development of BEV-centric methods, contributing to a gap in the literature.

Although BEVFusion moves toward more efficient multimodal fusion, it introduces a strong assumption: correct operation depends on sufficient spatial alignment across modalities. Recent methods such as LGMMFusion [23] and RoboFormer [24] show that integrating LiDAR can substantially improve agent-query-based models. At the same time, both approaches depend on explicit alignment in a shared BEV space. RoboFormer builds on the LSS lifting pipeline, whereas LGMMFusion introduces a specialized attention mechanism. Neither work explicitly discusses the additional latency introduced by the transformation.

Alternatively, simpler strategies [25], [26] process the visual modalities independently, preserving spatial self-attention while enabling cross-modal interaction at the semantic level. This combination of spatial and encoder-level alignment can improve downstream representations efficiently and can also increase model explainability. In particular, encoder-level attention allows the contribution of each modality to be inspected, helping assess when a modality is informative and identify difficult edge cases for the network.

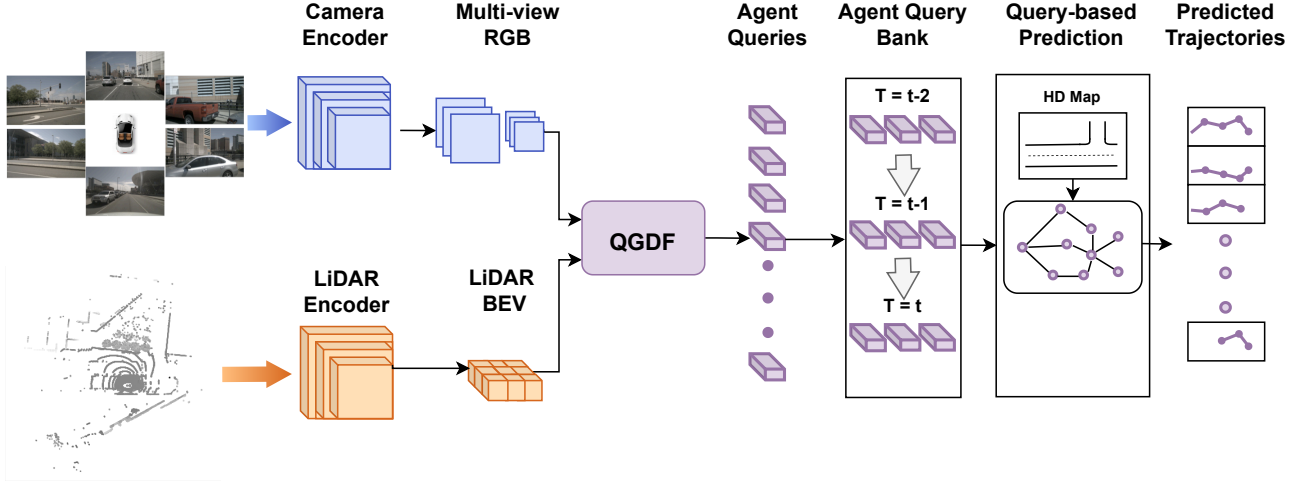


Fig. 1. Overall architecture of the Li-ViP3D++ multimodal end-to-end trajectory prediction model. The QGDF module is our primary contribution which handles sampling and fusion to ensure efficient usage of information from each input modality.

### III. METHODOLOGY

We expand the Li-ViP3D architecture, a multimodal network that enables end-to-end perception and prediction based on agent queries and uses separate encoders for processing each input modality and an attention mechanism for query-level feature fusion. Our approach is designed to exploit multimodality and attention-based fusion to drastically increase the quality of detected and predicted agents at a minimal increase in computational cost.

We use the large-scale nuScenes [27] dataset to train and evaluate the model while following the train/validation split as is standard for PnP solutions. The dataset contains 1000 scenes from urban scenarios with a duration of 20 seconds each. We utilize the data from the 6 RGB cameras sampled at 2Hz and 32-beam LiDAR sweeps at 10Hz and an HD map as input.

#### A. Feature extraction

The proposed multimodal model shown in Fig. 1 separately extracts 2D features from multi-view images as proposed by DETR3D using a ResNet50 [28] as a camera encoder backbone and processes multi-sweep LiDAR point cloud sweeps. We use 5 consecutive LiDAR sweeps (sampled at 10Hz) spanning 0.5s in a PointPillars [29] based LiDAR encoder. This allows us to perform hybrid fusion with several benefits. In addition to improving 3D detection accuracy, we improve the temporal reasoning of the model by vastly increasing the temporal density of input data. This can be achieved using a computationally simple encoder. In our configuration, the PointPillars encoder operates on points within [-51.2,51.2] meters in x/y axes and [-5,3] meters in the z axis. Points are discretized into pillars with voxel size (0.2,0.2,4.0), with up to 32 points per pillar, producing a dense BEV pseudo-image via pillar scattering. Each pillar is encoded by a single feed-forward network (FFN) layer (10-D point features  $\rightarrow$

64 channels) with BatchNorm and ReLU. The BEV map is then processed by a 3-stage 2D CNN backbone with stride 2 downsampling and channel widths 64,128,256, followed by a Feature Pyramid Network (FPN) style upsampling neck (deconvolutions with strides 1/2/4) that merges multi-scale features into a 256-channel BEV representation used for subsequent multimodal fusion.

We utilize a tracked agent query memory bank as described by ViP3D [6] and MOTR [30] to maintain information-dense historical feature states for each agent in the scene. Using agent queries, we can convert the feature representation to a space that allows for efficient object-level associations.

#### B. Modality fusion

At each time step, we update the representation of every agent query using our attention-based QGDF module. The overall flow of the QGDF mechanism is shown in Fig. 2.

Let  $Q_t \in \mathbb{R}^{N_q \times B \times E}$  denote the set of agent queries at time step  $t$ , and let  $r \in [0, 1]^{B \times N_q \times 3}$  be their associated normalized 3D reference points. We denote the multi-level image features by  $\{I^\ell\}_{\ell=1}^L$ , where each level  $I^\ell \in \mathbb{R}^{B \times N_{cam} \times E \times H_\ell \times W_\ell}$ , and we denote the LiDAR BEV features (when available) by  $P \in \mathbb{R}^{B \times E \times H_p \times W_p}$ .

*1) Image feature aggregation via masked attention over cameras and pyramid levels:* Rather than forming dot-product cross-attention between  $Q_t$  and dense image keys, we first sample image features at each query's reference point across all cameras and feature levels using a differentiable sampler. The sampling procedure projects  $r$  into each camera using the provided calibration matrices and applies bilinear sampling in each pyramid level, producing sampled features:

$$S = \text{Sample}(\{I^\ell\}, r) \in \mathbb{R}^{B \times E \times N_q \times N_{cam} \times 1 \times L}, \quad (1)$$

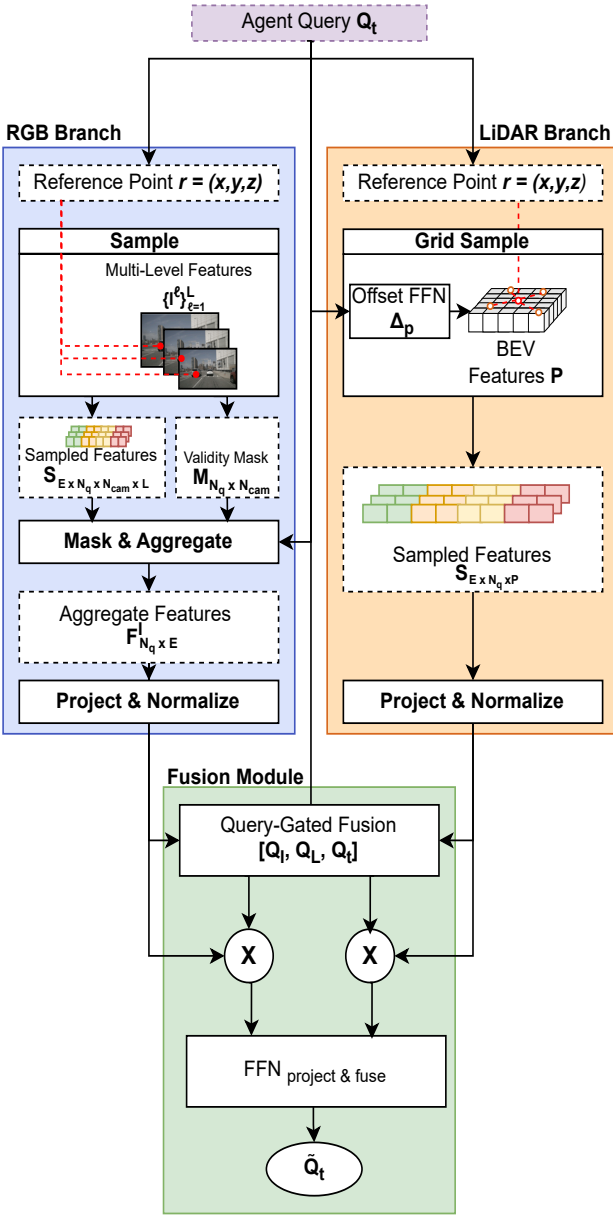


Fig. 2. Diagram of the Query-Gated Deformable Fusion (QGDF) mechanism and sampling from each modality.

The transformed reference points are also used to generate a validity mask:

$$M \in \{0, 1\}^{B \times 1 \times N_q \times N_{cam} \times 1 \times 1}, \quad (2)$$

which indicates whether the projected reference point lies in front of the camera and within image bounds. We then predict per-query attention logits over the camera-level combinations from the query features:

$$\omega^I = \text{FFN}_I(Q_t) \in \mathbb{R}^{B \times N_q \times (N_{cam}L)}. \quad (3)$$

To ensure that invalid views do not receive probability mass, we apply a masked softmax (using the expanded mask  $M$  across pyramid levels) to obtain normalized weights  $\alpha^I$ :

$$\alpha^I = \text{masked\_softmax}(\omega^I, M) \in \mathbb{R}^{B \times 1 \times N_q \times N_{cam} \times 1 \times L}. \quad (4)$$

Finally, we aggregate the sampled features across cameras and levels:

$$F^I = \sum_{n=1}^{N_{cam}} \sum_{\ell=1}^L \alpha_{n,\ell}^I S_{n,\ell} \in \mathbb{R}^{B \times E \times N_q}. \quad (5)$$

The resulting image features are projected and normalized to align them with the query embedding space, yielding  $\bar{Q}_t^I \in \mathbb{R}^{N_q \times B \times E}$ .

2) *LiDAR feature aggregation via differentiable BEV sampling*: We extract LiDAR context for each query by sampling  $P$  at the query's BEV reference location  $r_{xy}$  through a differentiable operator:

$$\bar{Q}_t^L = \text{BEVSample}(P, r_{xy}, Q_t) \in \mathbb{R}^{N_q \times B \times E}, \quad (6)$$

followed by feature normalization to match the image branch. If LiDAR input is not provided, we set  $\bar{Q}_t^L$  to zero.

Concretely, given a BEV LiDAR feature map  $P \in \mathbb{R}^{B \times C_L \times H \times W}$ , we first align it to the transformer embedding space using a  $1 \times 1$  convolution and spatial normalization, so that BEV features can be sampled and fused on the same  $E$ -dimensional scale as the image branch. For each query, we then predict 2D sampling offsets from its query embedding using a lightweight linear head:

$$\Delta_P = \text{FFN}(Q_t) \in \mathbb{R}^{B \times N_q \times P \times 2}, \quad (7)$$

where each  $\Delta_p$  corresponds to a learned local displacement in BEV space. The BEV reference coordinate  $r_{xy}$  (normalized to  $[0, 1]$ ) is mapped to the `grid_sample` coordinate system in  $[-1, 1]$ , and offsets are squashed and scaled to enforce a bounded search radius:

$$g = \text{clip}(g(r_{xy}) + s \cdot \tanh(\Delta_P), -1, 1), \quad (8)$$

We then sample  $P$  at the resulting per-query grid locations using bilinear interpolation with border padding,

$$S = \text{GridSample}(P, g) \in \mathbb{R}^{B \times N_q \times P \times E}, \quad (9)$$

which preserves gradient flow to both the BEV features and the predicted offsets. This procedure replaces hard  $k$ -selection with continuous, query-adaptive sampling and weighting, yielding a stable LiDAR context vector per query that can be fused with the image-derived representation. The resulting sampled LiDAR features are projected and normalized to align them with the query embedding space, yielding  $\bar{Q}_t^L \in \mathbb{R}^{N_q \times B \times E}$ .

3) *Query-aware gated multimodal fusion:* The modality contributions are combined using a query-conditioned gating mechanism. We compute fusion logits from the concatenation of normalized modality features and the (detached) query representation:

$$g_t = \text{FFN}_{\text{gate}}([\bar{Q}_t^I, \bar{Q}_t^L, Q_t]) \in \mathbb{R}^{N_q \times B \times 2}, \quad (10)$$

and obtain soft gates via

$$\gamma_t = \text{softmax}(g_t), \quad (11)$$

The gated modality features are then formed as

$$\hat{Q}_t^I = \gamma_{t,0} \bar{Q}_t^I, \quad \hat{Q}_t^L = \gamma_{t,1} \bar{Q}_t^L, \quad (12)$$

concatenated, and projected back to the query dimension:

$$\tilde{Q}_t = \text{FFN}_{\text{proj\&fuse}}([\hat{Q}_t^I, \hat{Q}_t^L]) \in \mathbb{R}^{N_q \times B \times E}. \quad (13)$$

4) *Residual update with positional encoding:* As in the original formulation, we incorporate a positional code derived from the reference points. Let  $\phi(\cdot)$  denote a lightweight position encoder; we compute

$$P_t = \phi(\text{inverse\_sigmoid}(r)) \in \mathbb{R}^{N_q \times B \times E}. \quad (14)$$

The updated query representation is then produced by a residual connection with dropout:

$$Q_{t+1} = \tilde{Q}_t + Q_t + P_t. \quad (15)$$

This procedure yields multimodally enhanced query representations that integrate camera evidence through masked attention over cameras and feature levels, LiDAR evidence through differentiable BEV sampling, and a query-conditioned gating mechanism that adaptively balances the two modalities.

### C. Agent Perception and Prediction

Utilizing this multi-stage feature update strategy allows all downstream operations and subtasks to be performed on substantially richer query representations. At each time step  $t$ , every enhanced but currently unassigned query is passed through a query decoder that predicts the query centre coordinates  $\hat{y}\sigma(i)$ . These query-level predictions are then used to construct a bipartite matching problem, where the pairwise cost between a ground-truth target  $y_i$  and a predicted query  $\hat{y}\sigma(i)$  combines classification confidence and bounding-box distance:

$$\begin{aligned} \mathcal{L}_{\text{match}}(y_i, \hat{y}\sigma(i)) = & -\mathbf{1}_{\{c_i \neq \emptyset\}} \hat{p}_{\sigma(i)}(c_i) \\ & + \mathbf{1}_{\{c_i \neq \emptyset\}} \mathcal{L}_{\text{box}}(b_i, \hat{b}_{\sigma(i)}) \end{aligned} \quad (16)$$

Here,  $\mathcal{L}_{\text{box}}$  denotes the  $l_1$  loss over bounding-box parameters,  $b_i$  is the ground-truth box, and  $\hat{b}_{\sigma(i)}$  together with  $\hat{p}_{\sigma(i)}(c_i)$  correspond to the predicted box and the predicted probability of class  $c_i$ , respectively. Queries that have already been matched to a ground-truth agent preserve this assignment across time, unless the query is predicted as empty. Such persistent assignments are removed from the pairwise cost matrix and are therefore not reconsidered during matching.

To carry temporal context through the query memory bank, we additionally apply a temporal cross-attention operation. For each agent query  $q_t^i$ , we attend to its own stored history in the memory bank and compute a compact temporal summary:

$$\tilde{q}_t^i = \text{softmax} \left( \frac{q_{t,\text{query}}^i \mathbf{Q}_{\text{bank, key}}^i}{\sqrt{d}} \right) \mathbf{Q}_{\text{bank, value}}^i. \quad (17)$$

Following MOTR [30], the query memory bank is implemented as a first-in-first-out queue. We store a fixed history of four previous time steps per query. This design enables efficient agent-level temporal processing by compressing the historical states associated with query  $q^i$  contained in  $Q_{\text{bank}}^i$ . Importantly, the temporal aggregation is performed independently for each query to improve computational efficiency and to prevent information leakage across different agents. The resulting query feature is obtained using a two-layer feedforward network:

$$q_t^{i'} = \text{FFN}(q_t^i + \tilde{q}_t^i), \quad (18)$$

thereby integrating the spatio-temporal information produced by the multimodal feature update stages.

For trajectory forecasting, we follow the established design choices of ViP3D. The resulting enhanced agent queries are further processed and fused with an HD semantic map encoded using VectorNet [31], which provides a vectorized representation of contextual road semantics, including lane structure, traffic signs, and related map elements. Final trajectory outputs are generated using a regression-based decoder implemented as a two-layer FFN, predicting  $K$  candidate trajectories per agent.

Consistent with the end-to-end, fully differentiable formulation, the network is trained with a joint objective that optimizes classification, bounding-box regression, and trajectory decoding simultaneously. The classification and bounding-box regression terms are computed as:

$$\mathcal{L}_{\text{cls}} = \sum i = 1^N - \log \hat{p}_{\hat{\sigma}(i)}(c_i), \quad (19)$$

$$\mathcal{L}_{\text{coord}} = \sum i = 1^N \mathbf{1}_{c_i \neq \emptyset} \mathcal{L}_{\text{box}}(b_i, \hat{b}_{\hat{\sigma}(i)}). \quad (20)$$

The regression-based trajectory decoding loss is defined as an  $l_1$  regression term,  $\mathcal{L}_{\text{reg}}$ , computed between the ground-truth future trajectory  $s$  and the best-matching predicted hypothesis  $s^{(\hat{k})}$ . Concretely, we evaluate the loss over the prediction horizon  $T_{\text{future}}$  as

$$\mathcal{L}_{\text{trajectory}} = \sum t = 1^{T_{\text{future}}} \mathcal{L}_{\text{reg}}(s_t, s_t^{(\hat{k})}). \quad (21)$$

The index  $\hat{k}$  is selected using a minimum-distance criterion: among the  $K$  predicted trajectories, we choose the one that minimizes the  $l_2$  distance to the ground truth when comparing all corresponding trajectory points. With this selection rule, the overall training objective becomes

$$\mathcal{L} = \mathcal{L}_{\text{cls}} + \mathcal{L}_{\text{coord}} + \mathcal{L}_{\text{trajectory}}. \quad (22)$$

TABLE I

PERFORMANCE COMPARISON BETWEEN TRADITIONAL, PNPNET-VISION, ViP3D AND OUR PROPOSED METHOD. LOWER IS BETTER FOR minADE, minFDE, AND MR; HIGHER IS BETTER FOR EPA.

Metrics	Det3D + Kalman Filter	PnPNet-vision [19]	ViP3D [6]	Li-ViP3D [9]	Li-ViP3D++ (Ours)
$minADE_k \downarrow$	2.07 m	2.04 m	1.52 m	<b>1.45 m</b>	1.57 m
$minFDE_k \downarrow$	3.10 m	3.08 m	2.35 m	<b>2.20 m</b>	2.53 m
$MR \downarrow$	0.289	0.277	0.239	<b>0.236</b>	0.264
$EPA \uparrow$	0.191	0.198	0.236	0.250	<b>0.335</b>
$FP \text{ ratio} \downarrow$	-	-	0.231	0.221	<b>0.147</b>
$Recall \uparrow$	-	-	0.469	0.458	<b>0.472</b>
$Precision \uparrow$	-	-	0.769	0.779	<b>0.852</b>
$mAP \uparrow$	-	-	0.472	0.472	<b>0.502</b>

#### IV. RESULTS

We evaluate the proposed fusion mechanism using a set of complementary detection and prediction metrics, selected to provide a robust view of overall system performance and to isolate the contribution of the fusion strategy.

For trajectory forecasting, we report minimum Average Displacement Error ( $minADE_k$ ) and minimum Final Displacement Error ( $minFDE_k$ ), which quantify the mean and final  $l_2$  distance, respectively, between predicted and ground-truth agent positions under the best-matching hypothesis among  $K$  outputs. We also include the Miss Rate ( $MR$ ), defined here as the fraction of predictions whose  $minFDE$  exceeds 2 meters. To capture end-to-end behavior in the presence of false positives, we also report End-to-end Prediction Accuracy (EPA) [6]. EPA explicitly accounts for false positives by matching predicted agents to ground truth based on spatial proximity and computing a normalized hit rate as the ratio of matched predictions to the total number of ground-truth agents.

As displacement errors and derived metrics are notoriously insufficient for evaluating end-to-end PnP models due to the low impact of incorrect detections on final results, we include a set of detection-focused metrics. These include *Precision*, *Recall*, *mAP*, and *FP ratio* (normalized average ratio of false positive detections per scene).

All experiments are conducted within a region spanning 51.2 meters in each direction and cover seven agent categories: car, truck, bus, trailer, motorcycle, bicycle, and pedestrian. Trajectories are evaluated over a forecasting horizon of  $\Delta T = 6$  seconds, and the model outputs  $K = 6$  candidate future trajectories per agent.

The primary comparison between our method and the considered baselines is reported in Table I. We evaluate against (i) a conventional modular pipeline that separates Perception and Prediction, (ii) a modified vision-based PnPNet variant, (iii) ViP3D, and (iv) the original Li-ViP3D. For consistency and to ensure a fair comparison, all methods employ a regression-based trajectory decoder. We also retrained the ViP3D architecture with the same setup and hardware as the multimodal architectures to make sure the comparisons are as accurate as possible. The retrained version achieved better displacement error metrics,  $minADE_k$  of 1.52 meters and  $minFDE_k$  of 2.35 meters, compared to the results published in the ViP3D

paper ( $minADE_k$  of 2.03 meters and  $minFDE_k$  of 2.90 meters)

While the proposed improved fusion mechanism for enhancement of agent queries leads to slightly worse displacement error performance compared to the Li-ViP3D and re-trained ViP3D architectures for the  $\Delta T = 6$  seconds prediction horizon, as used in the ViP3D evaluation protocol, our Li-ViP3D++ architecture achieves significantly better detection results on key metrics and end-to-end prediction accuracy.

The main benefits of the QGDF approach can be seen in the detection performance of the model. The proposed fusion achieves an absolute 8.5 % increase EPA, the most robust prediction metric, which is a relative improvement of 34%. This large improvement stems from a significant reduction in false positive detections. The ratio of hallucinated agents drops from an average of 22.1% in Li-ViP3D to 14.7%. This improvement tracks across all other detection metrics (*Precision*, *Recall*, and *mAP*), signifying the impact of our architectural improvements on the quality of detection outputs.

#### V. DISCUSSION

The results highlight a clear shift in the performance profile induced by the proposed fusion mechanism. Compared to the original Li-ViP3D, we trade a small amount of trajectory-displacement accuracy for substantially improved end-to-end behavior driven by stronger detection quality. This trade-off is particularly evident when comparing standard forecasting metrics ( $minADE/minFDE/MR$ ) against EPA and the explicit detection metrics. While the enhanced fusion slightly degrades  $minADE/minFDE$  relative to the original Li-ViP3D architecture, it meaningfully increases EPA and reduces false positives, indicating that the model is more conservative and better calibrated about which agents exist and should be tracked. In practical autonomy stacks, this tendency is often preferable. Hallucinated agents can trigger unnecessary braking or planning failures even if the predicted trajectories for true agents are accurate.

A key observation is that the benefits are consistent across categories and are reflected in both precision-oriented metrics (*Precision*, *FP ratio*) and recall-oriented metrics (*Recall*, *mAP*). This suggests that the new query enhancement does not merely suppress detections indiscriminately; rather, it improves the semantic and spatial alignment between predicted queries and

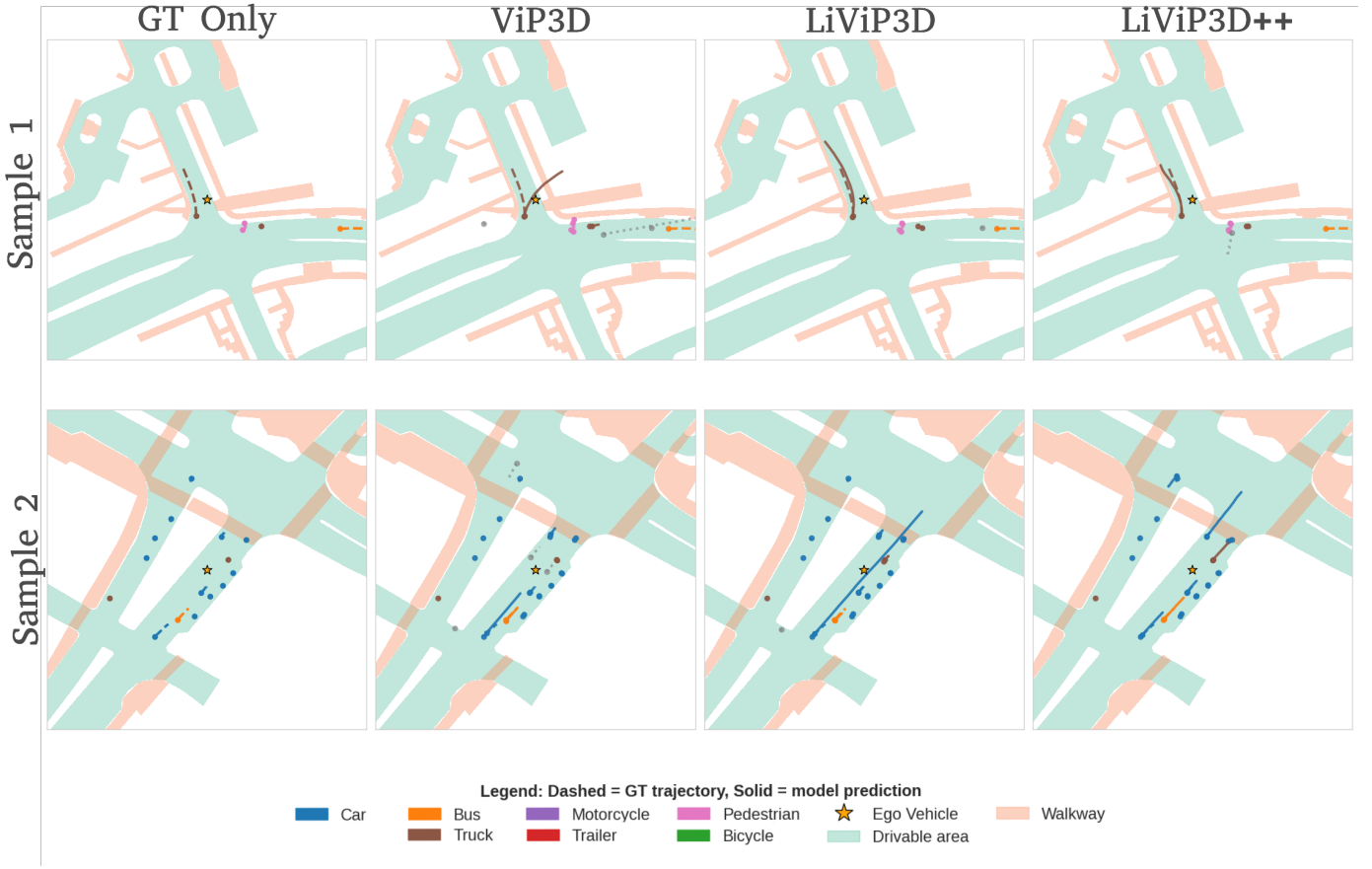


Fig. 3. Visual comparisons of the predicted trajectories for each of the compared agent query-based models. Each model predicted  $K=6$  possible future trajectories, we visualize the trajectory with the highest confidence for each sample.

real scene entities. The simultaneous increase in EPA and decrease in MR further supports that the outputs are better matched to ground truth in a way that persists into forecasting, not just detection. Although EPA gains may appear numerically modest, they correspond to a meaningful increase in correct matches per scene and can compound in dense traffic, where a small reduction in false positives and missed agents can significantly improve downstream planning stability.

#### A. Qualitative analysis

Qualitatively, we observe that the new enhanced fusion mechanism implies a trend of query grounding. Our model's outputs, as well as ground truth, and baseline predictions for comparison can be seen in Fig. 3 for two separate scenes. As the quantitative metrics imply, we see a significant decrease in both complete hallucinations and predictions marked as false positives due to the them being more than 2 meters away from the ground truth agent in the initial frame.

Despite the increase in overall displacement errors, the model predictions are reasonable and internally consistent. The model can handle more complex maneuvers while remaining in expected bounds based on the scene - vehicle agents tend to remain within drivable areas while pedestrians remain in walkways and crossings. We also observe an increase in

intra-agent consistency within scenes. As can be seen in Fig. 3, the model expects neighboring agents of the same class to be moving at a similar velocity. This leads to more consistent trajectories and fewer outliers. Overall, the new fusion mechanism leads to a better utilization of LiDAR data and thus a decrease in seemingly random trajectory length over-predictions.

#### B. Modality usage and reliance

The learnable modality fusion mechanism described in Section III-B let's us analyze the inferred reliance on LiDAR features within the enhanced queries. Overall, we observe that the model learned to utilize the LiDAR modality successfully. The mean usage of the lidar modality across all predicted agents in our testing data was 30%.

While the usage ratio of both modalities remains relatively stable across all scenes, two trends are notable. First, reliance on LiDAR varies by class: for example, the *truck* and *trailer* class exhibit an average LiDAR contribution of 28%, while motorcycles/bicycles show a higher contribution (31%). One plausible explanation is that smaller agents are more sensitive to appearance ambiguity and partial occlusions in RGB, so even modest LiDAR evidence can provide a stabilizing geometric cue that helps disambiguate true objects from clutter

while the larger *truck* and *trailer* are rarely ever significantly occluded in the RGB source data.

Second, the LiDAR contribution increases with point support. While outlier queries with fewer than 5 LiDAR points in the predicted bounding box area still show LiDAR reliance at an average of 27.1%, queries supported by more than 100 points rise to 31.1%. Every other measured bin (5-10, 10-20, ..., 90-100) showed a reliance between 29-30%.

This monotonic trend is consistent with an adaptive fusion behavior where the model strengthens geometric conditioning when reliable 3D evidence is available, which can directly reduce hallucinated detections. Importantly, the nonzero reliance even at very low point counts suggests that the model learns to exploit sparse LiDAR cues (e.g., a few returns at characteristic heights) without becoming brittle when LiDAR is weak.

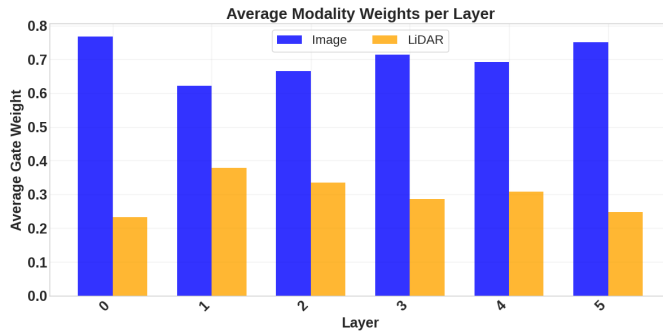


Fig. 4. Average weight of RGB and LiDAR modalities across all refinement layers of Li-ViP3D on testing data.

Our analysis also showed the importance of continuous refinement of agent queries as per the DETR3D protocol. Each transformer decoder layer is able to utilize a different ratio of modality information for adjusting agent query representations as shown in Fig. 4.

### C. Efficiency evaluation

TABLE II  
LATENCY COMPARISON (MEAN  $\pm$  STD) ACROSS METHODS, MEASURED IN MILLISECONDS. LOWER IS BETTER.

Method	Mean	Std	Min	Max
ViP3D	117.27	0.06	117.19	117.36
Li-ViP3D++	139.82	0.14	139.64	140.10
Li-ViP3D	145.91	0.36	145.56	146.69

Beyond accuracy, it is important for PnP to consider time-constraints of their applications. Table II reports the latency comparison of our end-to-end Li-ViP3D++ architecture. All compared architectures used ResNet50 as their image backbone, the multimodal architectures both used PointPillars with the same configuration as the LiDAR backbone. Resolution of input RGB images was 1600 x 900 pixels which is the default resolution used by ViP3D.

The proposed QGDF mechanism is faster than the original Li-ViP3D implementation (139.82 ms vs. 145.91 ms; a 6.09 ms reduction,  $\approx 4.4\%$ ), while remaining slower than

ViP3D (117.27 ms). This places the new fusion in a favorable position among LiDAR-vision PnP models: it improves the most deployment-relevant quality dimension (false positives / EPA) without increasing latency, and it slightly reduces runtime relative to the original multimodal baseline. The remaining gap to ViP3D is expected given the added multimodal processing and fusion steps, but it also motivates future work on compute-aware fusion (e.g., conditional modality usage or early-exit mechanisms). The evaluation was performed on a single NVIDIA GeForce RTX 4090 GPU and AMD Ryzen Threadripper PRO 7965WX CPU. We performed no performance optimizations (such as using TensorRT) on any of the models.

## VI. CONCLUSIONS AND FUTURE WORK

In this work, we introduced Query-Gated Deformable Fusion (QGDF), a query-space camera–LiDAR fusion mechanism that strengthens end-to-end perception and trajectory prediction. We apply QGDF to Li-ViP3D++, extending our prior Li-ViP3D architecture with differentiable LiDAR BEV sampling using learned per-query offsets and soft weighting, and query-adaptive modality gating that dynamically balances visual and LiDAR evidence. Together, these changes replace heuristic fusion and discrete top- $k$  selection with a fully differentiable, query-conditioned fusion process that is easier to optimize and more stable during training.

Through comprehensive evaluations on the nuScenes dataset, we demonstrate that Li-ViP3D++ significantly improves robust prediction quality metrics such as EPA, as well as improving the detection quality measured by mAP, Precision, Recall and False Positive detection ratios. Our results indicate that query-based multimodal representations provide a robust interface for jointly optimizing perception and prediction.

On nuScenes, Li-ViP3D++ achieves consistent gains in both end-to-end behavior and detection quality. In particular, it reaches an EPA of 0.335 while improving detection performance to 0.502 mAP, alongside higher Precision/Recall and a substantially lower false-positive ratio of 0.147. Importantly, these robustness and calibration improvements do not come at a latency penalty. Li-ViP3D++ is slightly faster than the original Li-ViP3D baseline (139.82 ms vs. 145.91 ms), supporting its practical deployability.

Some future work still remains, namely exploring the benefits that using multimodal agent queries bring in the context of constrained information sources by removing the dependence on HD maps, which can prove to be a limiting factor in many applications. Another potential benefit of multimodal agent queries that need to be explored is reducing the computational cost of end-to-end PnP solutions, by reducing the need for high-quality input sensor data. The multimodal agent query interface appears to be robust against reductions in quality and sensor noise. The proposed multimodal information sharing mechanism should also be evaluated to quantitatively determine the benefits it can bring under adverse conditions, such as lightning and weather variations.

## REFERENCES

- [1] N. Peri, J. Luiten, M. Li, A. Ošep, L. Leal-Taixé, and D. Ramanan, “Forecasting from lidar via future object detection,” in *Proceedings of the IEEE/CVF Conference on Computer Vision and Pattern Recognition*, 2022, pp. 17202–17211.
- [2] M. Bijelic, T. Gruber, F. Mannan, F. Kraus, W. Ritter, K. Dietmayer, and F. Heide, “Seeing through fog without seeing fog: Deep multi-modal sensor fusion in unseen adverse weather,” in *Proceedings of the IEEE/CVF Conference on Computer Vision and Pattern Recognition*, 2020, pp. 11682–11692.
- [3] A. Geiger, P. Lenz, and R. Urtasun, “Are we ready for autonomous driving? the kitti vision benchmark suite,” in *2012 IEEE conference on computer vision and pattern recognition*. IEEE, 2012, pp. 3354–3361.
- [4] N. Carion, F. Massa, G. Synnaeve, N. Usunier, A. Kirillov, and S. Zagoruyko, “End-to-end object detection with transformers,” in *European conference on computer vision*. Springer, 2020, pp. 213–229.
- [5] Y. Wang, V. C. Guizilini, T. Zhang, Y. Wang, H. Zhao, and J. Solomon, “Detr3d: 3d object detection from multi-view images via 3d-to-2d queries,” in *Conference on Robot Learning*. PMLR, 2022, pp. 180–191.
- [6] J. Gu, C. Hu, T. Zhang, X. Chen, Y. Wang, Y. Wang, and H. Zhao, “Vip3d: End-to-end visual trajectory prediction via 3d agent queries,” in *Proceedings of the IEEE/CVF Conference on Computer Vision and Pattern Recognition*, 2023, pp. 5496–5506.
- [7] A. L. F. Comeca, N. Masarykova, M. Halinkovic, M. Galinski, P. Laskov, and A. Vinel, “Social robots for road safety: Pedestrian crossing assistance use-case,” in *2025 International Symposium ELMAR*. IEEE, 2025, pp. 53–56.
- [8] ———, “Robots for safer pedestrian crossing on two-lane roads,” in *2025 IEEE International Automated Vehicle Validation Conference (IAVVC)*. IEEE, 2025, pp. 1–6.
- [9] M. Halinkovic, A. Vinel, and W. Benesova, “Li-vip3d: Enhancing end-to-end perception and prediction with camera-lidar fusion,” in *2025 IEEE International Automated Vehicle Validation Conference (IAVVC)*. IEEE, 2025, pp. 1–6.
- [10] Y. Huang, J. Du, Z. Yang, Z. Zhou, L. Zhang, and H. Chen, “A survey on trajectory-prediction methods for autonomous driving,” *IEEE Transactions on Intelligent Vehicles*, vol. 7, no. 3, pp. 652–674, 2022.
- [11] Y. Xu, E. Zablocki, A. Boulch, G. Puy, M. Chen, F. Bartoccioni, N. Samet, O. Simeoni, S. Gidaris, T.-H. Vu *et al.*, “Valeo4cast: A modular approach to end-to-end forecasting,” *arXiv preprint arXiv:2406.08113*, 2024.
- [12] Z. Wang, F. Chen, K. Lertniphonphan, S. Chen, J. Bao, P. Zheng, J. Zhang, K. Huang, and T. Zhang, “Technical report for argoverse challenges on unified sensor-based detection, tracking, and forecasting,” *arXiv preprint arXiv:2311.15615*, 2023.
- [13] J. Woo, J. Kim, and S. Im, “Motion forecasting via coordinate transformations and object trajectory modifications,” Technical report, 2023. 4, Tech. Rep., 2023.
- [14] Y. Xu, L. Champon, É. Zablocki, M. Chen, A. Alahi, M. Cord, and P. Pérez, “Towards motion forecasting with real-world perception inputs: Are end-to-end approaches competitive?” in *2024 IEEE International Conference on Robotics and Automation (ICRA)*. IEEE, 2024, pp. 18428–18435.
- [15] N. Masarykova, M. Galinski, and P. Truchly, “Single-filter cnn for vehicle recognition,” in *2024 International Symposium ELMAR*. IEEE, 2024, pp. 5–8.
- [16] M. Galinski, V. Danylov, P. Lehoczky, R. Bencel, and L. Soltes, “Ultra-fast visible lane distance estimation using a single camera,” *IEEE Access*, 2024.
- [17] W. Luo, B. Yang, and R. Urtasun, “Fast and furious: Real time end-to-end 3d detection, tracking and motion forecasting with a single convolutional net,” in *Proceedings of the IEEE conference on Computer Vision and Pattern Recognition*, 2018, pp. 3569–3577.
- [18] S. Casas, W. Luo, and R. Urtasun, “Intentnet: Learning to predict intention from raw sensor data,” in *Conference on Robot Learning*. PMLR, 2018, pp. 947–956.
- [19] M. Liang, B. Yang, W. Zeng, Y. Chen, R. Hu, S. Casas, and R. Urtasun, “Pnpnet: End-to-end perception and prediction with tracking in the loop,” in *Proceedings of the IEEE/CVF Conference on Computer Vision and Pattern Recognition*, 2020, pp. 11553–11562.
- [20] W. Zeng, W. Luo, S. Suo, A. Sadat, B. Yang, S. Casas, and R. Urtasun, “End-to-end interpretable neural motion planner,” in *Proceedings of the IEEE/CVF Conference on Computer Vision and Pattern Recognition*, 2019, pp. 8660–8669.
- [21] Z. Liu, H. Tang, A. Amini, X. Yang, H. Mao, D. L. Rus, and S. Han, “Bevfusion: Multi-task multi-sensor fusion with unified bird’s-eye view representation,” in *2023 IEEE international conference on robotics and automation (ICRA)*. IEEE, 2023, pp. 2774–2781.
- [22] J. Philion and S. Fidler, “Lift, splat, shoot: Encoding images from arbitrary camera rigs by implicitly unprojecting to 3d,” in *Computer Vision–ECCV 2020: 16th European Conference, Glasgow, UK, August 23–28, 2020, Proceedings, Part XIV 16*. Springer, 2020, pp. 194–210.
- [23] H. Cheng, C. Liu, W. Gu, Y. Wu, M. Zhao, W. Liu, and N. Wang, “Lgmmfusion: A lidar-guided multi-modal fusion framework for enhanced 3d object detection,” *PloS one*, vol. 20, no. 9, p. e0331195, 2025.
- [24] Y. Liu, D. Liao, M. Qi, L. Liu, and H. Ma, “Roboformer: A robust multi-modal transformer for 3d object detection in autonomous driving,” in *Proceedings of the 6th ACM International Conference on Multimedia in Asia*, 2024, pp. 1–7.
- [25] M. Halinkovic, O. Fabian, A. Felsoova, M. Kveton, and W. Benesova, “Intrinsically explainable deep learning architecture for semantic segmentation of histological structures in heart tissue,” *Computers in Biology and Medicine*, vol. 177, p. 108624, 2024.
- [26] T. Brödermann, C. Sakaridis, Y. Fu, and L. Van Gool, “Cafuser: Condition-aware multimodal fusion for robust semantic perception of driving scenes,” *IEEE Robotics and Automation Letters*, 2025.
- [27] H. Caesar, V. Bankiti, A. H. Lang, S. Vora, V. E. Liang, Q. Xu, A. Krishnan, Y. Pan, G. Baldan, and O. Beijbom, “nuscenes: A multimodal dataset for autonomous driving,” in *Proceedings of the IEEE/CVF conference on computer vision and pattern recognition*, 2020, pp. 11621–11631.
- [28] K. He, X. Zhang, S. Ren, and J. Sun, “Deep residual learning for image recognition,” in *Proceedings of the IEEE conference on computer vision and pattern recognition*, 2016, pp. 770–778.
- [29] A. H. Lang, S. Vora, H. Caesar, L. Zhou, J. Yang, and O. Beijbom, “Pointpillars: Fast encoders for object detection from point clouds,” in *Proceedings of the IEEE/CVF conference on computer vision and pattern recognition*, 2019, pp. 12697–12705.
- [30] F. Zeng, B. Dong, Y. Zhang, T. Wang, X. Zhang, and Y. Wei, “Motr: End-to-end multiple-object tracking with transformer,” in *European Conference on Computer Vision*. Springer, 2022, pp. 659–675.
- [31] J. Gao, C. Sun, H. Zhao, Y. Shen, D. Anguelov, C. Li, and C. Schmid, “Vectornet: Encoding hd maps and agent dynamics from vectorized representation,” in *Proceedings of the IEEE/CVF conference on computer vision and pattern recognition*, 2020, pp. 11525–11533.